ChemPubSoc Europe

DOI: 10.1002/celc.201902005

CHEMELECTROCHEM Articles

$PrFeO_3$ Photocathodes Prepared Through Spray Pyrolysis

Emma Freeman,[a, c] Santosh Kumar,[a, d] Sophie R. Thomas,[a, c] Hayley Pickering,[a] David J. Fermin,[b] and Salvador Eslava*[a, d]

Perovskite oxides are receiving wide interest for photocatalytic and photoelectrochemical devices, owing to their suitable band gaps for solar light absorption and stability in aqueous applications. Herein, we assess the activity of $PrFeO_3$ photocathodes prepared by using spray pyrolysis and calcination temperatures between 500 and 700 °C. Scanning electron microscopy shows corrugated films of high surface coverage on the conductive glass substrate. The electrochemically active surface area shows slight decreases with temperature increases from 500 to 600 and 700 °C. However, transient photocurrent responses and impedance spectroscopy data showed that films calcined at higher temperatures reduced the probabilities of recombination due to trap states, resulting in faster rates of charge extraction. In this trade-off, a calcination temperature of 600 °C provided a maximum photocurrent of -130 ± 4 μA cm^{-2} at +0.43 V_{RHE} under simulated sunlight, with an incident photon-to-current conversion efficiency of 6.6% at +0.61 V_{RHE} and 350 nm and an onset potential of +1.4 V_{RHE} for cathodic photocurrent.

1. Introduction

To reduce our reliance on the burning of carbon-based fossil fuels more attention is needed on clean alternatives such as hydrogen. Hydrogen can be burnt as a fuel or oxidized in fuel cells to generate electricity, producing just water as a by-product.[1] Currently, most of the production of hydrogen relies on methane steam reforming which readily emits CO_2 into the atmosphere.[2] Photoelectrochemical (PEC) water-splitting is considered as an alternative route for sustainable hydrogen production. This process consists of splitting of water into O_2 and H_2 promoted by photogenerated charge carriers in semiconductors, as originally demonstrated in the seminal work by Fujishima and Honda.[3]

There is a range of metal oxide semiconductors capable of driving PEC reactions in addition to the typical TiO_2 and $SrTiO_3$ semiconductors.[4,5] Hematite (α-Fe_2O_3) for example has been well studied as a photoanode[6] but commonly suffers from high levels of electron-hole recombination.[7] Additionally, $BiVO_4$ and WO_3 have been well studied.[8,9] Other general limitations of metal oxides include poor carrier collection and poor light absorption.[10] Hence, further development on improving the efficiency and scope of these materials are needed especially with a focus on p-type photocathodes to replace expensive Pt cathodes which do not offer light absorption.

Various p-type semiconductor light absorbers have been investigated.[11] For example Cu_2O and $CaFe_2O_4$ both exhibit good photocathodic responses.[12,13] However, with Cu_2O in particular, there are limitations due to poor photostability. Due to this problematic inherent instability, the application of protection layers is needed to allow it to be a viable and practical material.[14,15] Additionally, Cu_2S photocathodes have been shown to be very promising for solar hydrogen evolution with the addition of a TiO_2 protection layer.[16] Hence, it is advantageous to investigate p-type metal oxides that exhibit increased stability to prevent the need for additional protection layers. It is therefore wise to draw attention to perovskite compounds (ABX_3), that have shown to be successful in a range of PEC processes such as organic dye degradation, water splitting and within photovoltaics.[17] Organo lead trihalides (e.g. $CH_3NH_3PbI_{3-x}Cl_x$.) have been especially popular in the field of solid-state solar cells where their use is widespread.[18] However, they fall short in their application for water splitting due to inherent instabilities in water, although work has been done to combat this.[19,20]

Perovskite oxides (ABO_3) on the other hand are water stable and non-toxic and have demonstrated activity for water splitting reactions.[21] Additional benefits include abundant starting materials and high levels of structural flexibility.[22] In a previous article, we have reviewed the use of different perovskite oxides for photocatalytic and PEC applications.[23] Many required the use of metal doping to allow for a reduction of band gap to assist in visible light absorption, such as in the cases of Bi-$NaTaO_3$ and Rh-$SrTiO_3$ that have both shown activity for water reduction.[24,25] On the other hand, ferrite-based

[a] E. Freeman, Dr. S. Kumar, S. R. Thomas, H. Pickering, Dr. S. Eslava
Department of Chemical Engineering
University of Bath
Claverton Down, Bath, BA2 7AY (UK)
E-mail: s.eslava@imperial.ac.uk
[b] Prof. Dr. D. J. Fermin
School of Chemistry
University of Bristol
Cantock's close, Bristol, BS8 1TS (UK)
[c] E. Freeman, S. R. Thomas
EPSRC Centre for Doctoral Training in Catalysis
School of Chemistry, Cardiff University
Park Place, Cardiff, CF10 3AT (UK)
[d] Dr. S. Kumar, Dr. S. Eslava
Department of Chemical Engineering
Imperial College London
South Kensington, London, SW7 2AZ (UK)

Supporting information for this article is available on the WWW under https://doi.org/10.1002/celc.202902005

perovskite oxides have smaller band gaps and hence avoid the use of doping to enhance visible-light absorption. $BiFeO_3$ (BFO) has shown to be active for PEC processes and has a measured band gap of 2.3 eV, which encompasses the visible-light region.[26] Due to the large Bi^{3+} ions in BFO they are able to induce strain within the perovskite structure, that can alter electronic structure which in turn is able to dictate p and n-type character.[27,28] $LaFeO_3$ (LFO) has also shown p-type behavior with an ideal band gap of ~2.1 eV and has shown to be active in dye degradation,[29] oxygen reduction and water reduction.[30,31] Photocurrents for bare LFO have reached around $-160\ \mu A\,cm^{-2}$ at $+0.26\ V_{RHE}$ using a spray pyrolysis synthesis method or $-161\ \mu A\,cm^{-2}$ at $+0.43\ V_{RHE}$ using a polymer templating method.[32,23] An electrodeposited film achieved $-124\ \mu A\,cm^{-2}$ for bare LFO, which increased to $-268\ \mu A\,cm^{-2}$ at $+0.6\ V_{RHE}$ on K-doping in O_2 purged electrolyte.[31] Similarly to BFO, in some instances LFO has shown activity for water oxidation, where on doping with Cu a photocurrent density of $+0.99\ mA\,cm^{-2}$ was reported, displaying the bi-polar p and n-conductivity.[33] Additionally, $YFeO_3$ photocathodes have also demonstrated activity for hydrogen evolution, further demonstrating the successful application of ferrite perovskites for water splitting reactions.[34]

Another, more understudied ferrite perovskite, is $PrFeO_3$ (PFO), which has been previously reported as a material in sensing applications such as for CO_2 and nitrite detection.[35,36] It has also been demonstrated to be active for the decomposition of methyl orange under visible light irradiation, displaying a band gap of 2.4 eV.[37] Additionally, PFO has also shown activity for photocatalytic hydrogen generation from an ethanol/water solution with visible light illumination.[38] In this case, PFO was synthesized using a sol-gel, template and combustion method with measured band gaps between 1.88 and 2.08 eV. In particular, the sol-gel method involved synthesis of PFO using praseodymium nitrate hexahydrate, ferrite nitrate nonahydrate and citric acid, which produced crystallite sizes of 20 nm after calcination at 700 °C. Whilst incorporating a Pt-cocatalyst, this PFO powder generated hydrogen at $2847\ \mu mol\,g^{-1}\,h^{-1}$.[38]

In this paper, for the first time to the best of our knowledge, the photoelectrochemical properties of PFO thin films are investigated. These PFO films are obtained through spray pyrolysis using a solution of nitrate-based precursors directly deposited onto a transparent conductive substrate. An optimized photocurrent density of $-130\pm4\ \mu A\,cm^{-2}$ at $+0.43\ V_{RHE}$ was achieved for PFO films calcined at 600 °C with a determined incident photon-to-current conversion efficiency (IPCE) of 6.6% at $+0.61\ V_{RHE}$ and 350 nm and a potential onset of $+1.4\ V_{RHE}$ for cathodic photocurrent. RC limited transients revealed that higher calcination temperatures of 600 and 700 °C showed faster rates of charge separation than that of 500 °C.

2. Results and Discussion

It has been previously shown that metal oxide films can be prepared through calcination of precursor solutions upon a desired substrate,[39] forming nanoparticles directly on the FTO. This can assist in enhancing contact between the metal oxide particles and the conductive back contact of the substrate. This process also reduces the number of heating steps and hence minimizes opportunities for particle sintering and loss of surface area. Therefore, this method was chosen to fabricate PFO films through depositing a solution of iron and praseodymium nitrates with citric acid in water onto aluminoborosilicate glass coated with fluorine-doped tin oxide (FTO-ABS), using spray pyrolysis, and then subsequently calcining at 500, 600 and 700 °C to form films PFO_500 °C, PFO_600 °C and PFO_700 °C.

X-ray diffraction (XRD) spectra confirm the formation of orthorhombic PFO directly onto the substrate for PFO_600 °C and PFO_700 °C. No PFO diffraction peaks were observed for a calcination temperature of 500 °C, which could demonstrate an absence of the formation of PFO on the FTO-ABS or simply a lack of crystallinity (Figure 1). Using the Scherrer equation, the coherent crystal domain sizes were determined for calcination temperatures of 600 and 700 °C to be 25 and 30 nm, respectively. X-ray photoelectron spectroscopy (XPS) measurements were obtained for all PFO films which further confirmed the presence of PFO for PFO_600 °C and PFO_700 °C and established the presence of PFO on the substrate for PFO_500 °C (Supporting Information Figure S1). Figure S1a and 1b show binding energies corresponding to Pr $3d_{5/2}$ (932.8 eV), Pr $3d_{3/2}$ (953.4 eV), Fe $2p_{3/2}$ (710.2 eV) with satellite (717.9 eV) and Fe $2p_{1/2}$ (723.9 eV). Figure S1c corresponds to both crystal lattice oxygen (O_L) and hydroxyl oxygen (O_H). The O_L signal at 529.1 eV can be associated with Pr—O and Fe—O contributions from the PFO crystal lattice. The signal at 531.2 eV can be attributed to hydroxyl groups from chemisorbed water. CasaXPS software was used to determine the Pr:Fe ratio for these PFO films which was 1:(0.7–0.8), showing between 20 and 30% A-site surface enrichment at all temperatures (Table S1). A-site surface segregation is commonly observed in perovskite oxide materials obtained by calcination of molecular precursors, showing a very complex dependence of the nature of the A and B sites[34,40–43] and temperature.[44] The Pr surface excess can play a

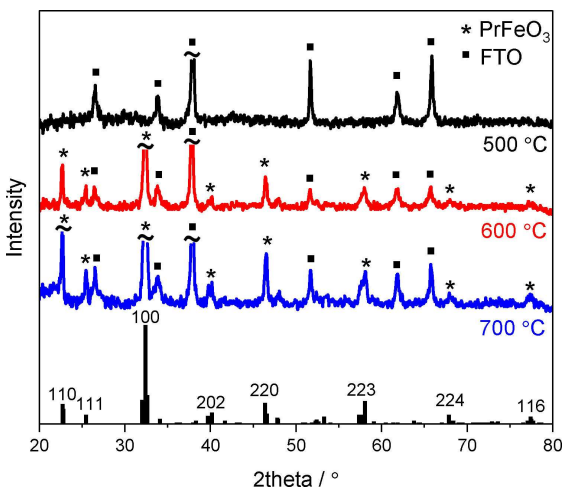

Figure 1. X-ray diffraction patterns of PFO films calcined at 500, 600 and 700 °C with standard $PrFeO_3$ XRD pattern.

role in charge extraction, although this issue is not assessed in this work.

Tauc plots generated from UV-Vis spectra (Figure S2) were analyzed assuming direct allowed optical transition ($n=1/2$) and a direct forbidden transition ($n=3/2$).[45] We have contrasted both cases given the little knowledge on the optical properties of these materials and the large degree of polycrystallinity of these PFO films. Analysis shows band gap values ranging from 1.7–2.1 eV with an average of 1.9 eV for these PFO thin films regardless of the calcination temperature (Figure S2). These values lie within the visible light region and are consistent with previously reported values (2.08 eV).[38]

Figure 2 shows field-emission scanning electron microscopy (FE-SEM) micrographs of the various PFO films. In all films, there appears to be good coverage upon the FTO surface with no FTO being visible at a magnification of 1 k. Even at an increased magnification of 15 k, for PFO_500 °C especially, there is no exposed FTO, with just small portions being visible for PFO_600 °C and _700 °C. In reference to morphology characteristics, PFO_500 °C shows a distinct lack of porosity that would reduce the level of contact between the electrolyte and PFO particles. Additionally, the PFO displays a cracked appearance with limited uniformity and high surface roughness (Figure 2a and b). On increasing calcination temperature to 600 °C, this cracked appearance remains, with some areas of FTO becoming visible. There is also a notable increase in porosity, which can be advantageous in maximizing semiconductor/electrolyte interactions due to this prevailing porosity allowing for an increase in surface area (Figure 2c and d). When the calcination temperature is increased further to 700 °C this observed porosity remains with very little exposed FTO being visible. Overall, it appears that all fabricated PFO films exhibit good levels of surface coverage on the glass substrate, which enables maximization of available surface area. There appears to be high surface roughness in all cases, with calcination temperatures exceeding 600 °C resulting in greater levels of porosity.

HR-TEM micrographs were also obtained to confirm the crystal phases of the calcined $PrFeO_3$. It can be seen in Figure 3a that PFO_500 °C appears amorphous in nature showing no crystallinity, which is confirmed also by the surface area diffraction (SAED) pattern which did not show any characteristic diffraction circles. This is as expected due to the failure in obtaining an XRD pattern at this calcination temperature, confirming this lack of crystallinity (Figure 1). PFO_600 °C showed a defined lattice structure under HR-TEM as seen in Figure 3b, with SAED demonstrating a d-spacing of 0.27 nm which corresponds to the (202) plane as determined from XRD using Bragg's law. PFO_700 °C also displays polycrystallinity under HR-TEM with determined d-spacing of 0.27 and 0.39 nm corresponding to the PFO planes (202) and (223) (Figure 3c). This in agreement with interplanar distances determined in the literature.[46]

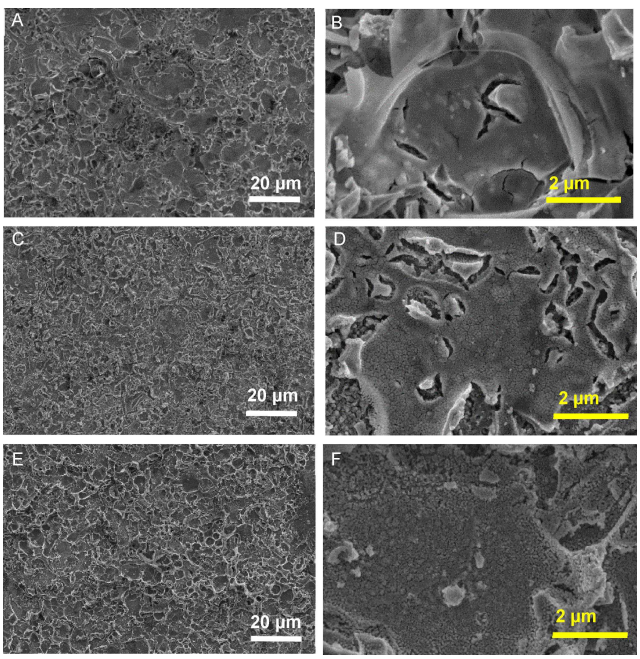

Figure 2. FE-SEM images of PFO films on FTO-ABS glass prepared through spray pyrolysis calcined at A, B) 500 °C, C, D) 600 °C and E, F) 700 °C.

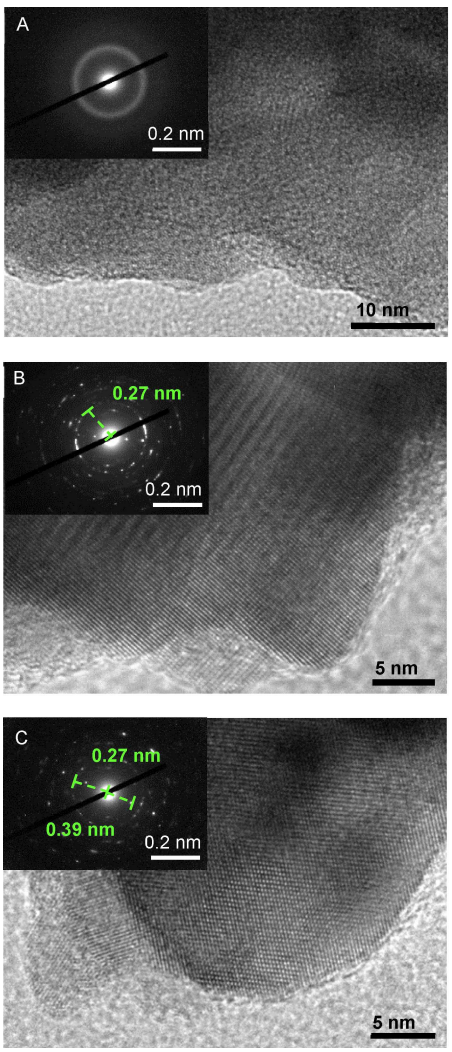

Figure 3. HR-TEM images of A) PFO_500 °C, B) PFO_600 °C and C) PFO_700 °C with SAED inserts including d-spacing determination.

Electrochemically active surface area (ECSA) measurements were obtained to assess any changes in active surface area between films. CV measurements were done in the dark with the capacitive current densities recorded at $-0.03\ V_{AgCl}$ ($+0.88\ V_{RHE}$) for different scan rates (Figure S3). Current densities were then plotted versus scan rate, where the gradient is proportional to ECSA (Figure 4). There are decreases in ECSA on the increasing of calcination temperature with values of 0.085, 0.072 and 0.058 $mF\,cm^{-2}$ for 500, 600 and 700 °C, respectively. This can be explained due to higher levels of sintering on the application of higher temperatures. A higher surface area film could be beneficial, as long as this does not result in increased recombination sites, in order to create a greater contact between the PFO particles and the electrolyte. Therefore, one could argue films should be annealed at temperatures below 500 °C, as it is typically done for other semiconductors such as WO_3, CuO and Cu_2O.[47,48] However, a lower calcination temperature of 500 °C has previously shown to be insufficient in producing detectable levels of crystalline PFO (Figure 1). Hence, a higher determined surface area in this case would not necessarily indicate a greater photoelectrocatalytic activity, despite the usual benefits that high ECSA could provide.

PEC responses were recorded using a three-electrode system with a 0.1 M Na_2SO_4 electrolyte (pH 12), under chopped simulated sunlight at 1 sun. Firstly, the optimum number of calcined PFO layers was determined so that a maximized photocurrent could be achieved. Up to 4 calcined PFO layers were applied and calcined at a temperature of 600 °C, and then tested for the ability to generate photocurrent. For 1, 2, 3 and 4 applied layers photocurrent densities of -64 ± 11, -113 ± 7, -130 ± 4 and $-122\pm5\ \mu A\,cm^{-2}$ at $+0.43\ V_{RHE}$ were achieved (Figure S4). Three calcined PFO layers was optimal for photocurrent and hence was used subsequently. Films PFO_500 °C, PFO_600 °C and PFO_700 °C were all prepared using three calcined layers and then photocurrent density was determined to establish optimal calcination temperature. Photocurrent densities of -17 ± 4, -130 ± 4 and $-101\pm2\ \mu A\,cm^{-2}$ at $+0.43\ V_{RHE}$ was achieved for PFO_500, 600 and 700 °C respectively (Figure 5a and b). IPCE measurements were also undertaken which showed efficiencies of 1.2, 6.6 and 2.7% at $+0.61\ V_{RHE}$ and 350 nm for calcination temperatures of 500, 600

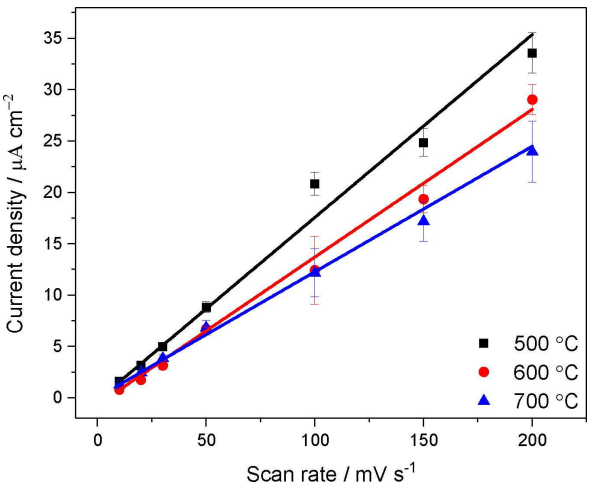

Figure 4. Capacitive current density vs. scan rate plots for films PFO films calcined at 500, 600 and 700 °C.

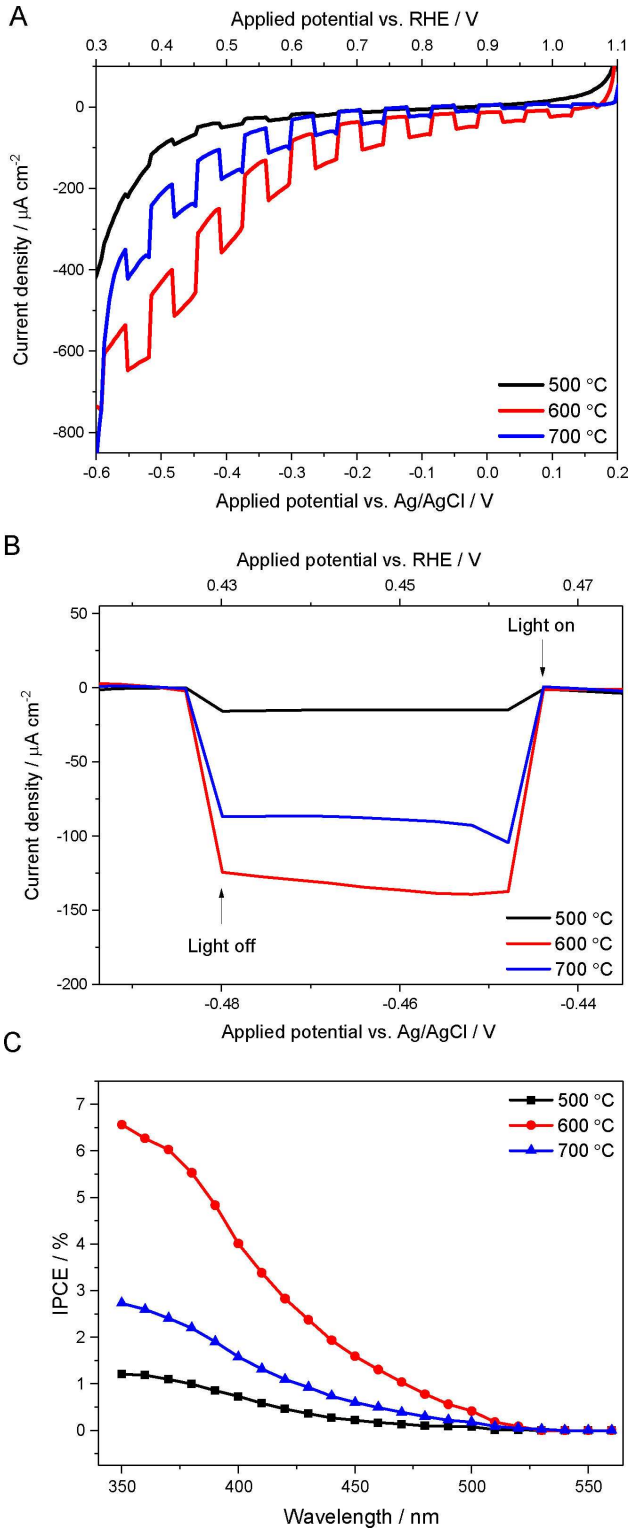

Figure 5. A) Current density vs. potential plots for PFO films calcined at 500, 600 and 700 °C measured under chopped simulated sunlight (AM 1.5 G, 100 $mW\,cm^{-2}$) in pH 12 0.1 M Na_2SO_4. B) Normalized current-potential measurements at point of interest +0.42 to +0.47 V_{RHE}. C) IPCE measurements at $+0.61\ V_{RHE}$ for PFO_600 °C.

and 700 °C respectively (Figure 5c). These relatively low efficiencies could suggest a poor level of charge separation and transport within the PFO and hence should be addressed in future work. A calcination temperature of 600 °C provided both the highest photocurrent density and IPCE, indicating that this is the optimum calcination temperature for these PFO films. A stability measurement was then completed for PFO_600 °C with chopped simulated sunlight at 1 sun for 1 h. It was seen that, after an initial stabilization, 96% of the photocurrent was maintained for this 1 h chopped measurement, displaying high levels of stability (Figure S5).

Additionally, it can be noted that for all PFO films there is a high onset potential demonstrated at $+1.4\ V_{RHE}$ for cathodic photocurrent (Figure S6). The increase in photocurrent observed for PFO_600 °C can be attributed to its high ECSA and importantly to its crystallinity, since PFO_500 °C has similar ECSA but no PFO XRD peaks were identified and then a low photocurrent was observed. For PFO_700 °C, the crystallinity is actually better (the calculated coherent domain size from the XRD spectra were 25 and 30 nm for PFO_600 °C and PFO_700 °C, resp.), but the ECSA values were lower due to sintering (0.072 and 0.058 mF cm^{-2}, resp.) reducing the ability of charge transfer and in this situation a lower photocurrent and IPCE values were achieved. Hence, there might be increased levels of detrimental sintering at this temperature.

Notably, from all the PEC measurements recorded in unpurged electrolyte that is exposed to air, there is a considerable dark current present, especially at potentials below $+0.4\ V_{RHE}$. Previous work has attributed this to the oxygen reduction reaction (ORR) upon exposed areas of FTO.[34] When light is irradiated, ORR is also expected with the photogenerated electrons, hence all the photocurrent cannot be assigned to the hydrogen evolution reaction (HER).[49,50] This can be demonstrated with purging of the electrolyte with N_2, where a decrease in photocurrent of 79% and visible reduction of dark current was seen (Figure S7), which suggests increased recombination without the presence of O_2. Additionally, there could be a further hindrance concerning competition for hole collection at the back contact, as seen with $LaFeO_3$ films. In this case, holes can accumulate at the semiconductor/electrolyte interface and take part in the oxygen evolution reaction (OER), increasing majority carrier losses. To combat this a hole-blocking layer could be employed.[51] Despite this observed vast reduction in photocurrent on purging the electrolyte with N_2, we were able to detect H_2 over a 6 h period with constant light illumination (Figure S8). This demonstrates these PFO photocathodes are able to reduce water and are stable over a long period of continuous illumination, however charge recombination remains a key limitation. Future work is needed to address such problematic competitive PEC processes and improve the selectivity for HER using co-catalysts and hole blocking layers if the purpose is storing solar energy in hydrogen bonds.

To better understand the differences in activity seen on changing calcination temperature, charge transport properties of these films were investigated. This was done by calculating the RC limited photocurrent transients for each PFO film from electrochemical impedance spectroscopy (EIS) measurements, and then comparing this with experimental transients to determine rise time (t). Smaller rise times are preferable as they can elude to greater efficiencies in charge transport. Figure 6a shows the EIS measurements in the dark at $+0.61\ V_{RHE}$ for each PFO film, with the corresponding plots comparing RC limited transients with experimental transients in Figure 6b–d. The rise time is the time in which it takes the maximum experimental photocurrent to reach the maximum photocurrent from the RC limited transient. Hence, rise time can be used to reveal charge transport characteristics of the material being studied. Rise times were determined to be 1.25, 0.17 and 0.13 s for PFO calcined at 500, 600 and 700 °C respectively. PFO_500 °C demonstrates the slowest rise time of 1.25 s which eludes to higher probabilities of recombination due to an increased density of trap states. Faster rise times were achieved for calcination temperatures of 600 and 700 °C, which can indicate faster rates of charge extraction in these films. This is in support of the enhanced photocurrent and IPCE achieved for these films (Figure 5c). Hence, it can be postulated that at a lower calcination temperature of 500 °C there are more defects that allow for a higher density of trap states to be present, leading to poor charge separation and increased recombination. At higher temperatures on the other hand, the presence of defect states is reduced, leading to better charge separation, explaining faster rise times observed. The fast rise times result in optimal photocurrents for samples calcined at 600 °C. Although 700 °C calcination leads to even faster rise times, this does not result in better photocurrents because sintering reduces the ECSA as seen in Figure 4. There is therefore a trade-off between rise time and ECSA.

Additionally, these EIS measurements were used to construct Mott-Schottky plots for the best performing PFO_600 °C in order to determine both the carrier (hole) density and flat band potential (V_{fb}). Caution is herein required due to the uncertain and large relative permittivity of ferrites, in this case 10^4,[52] and complex capacitive behaviors associated with porous films.[53] Actually, the variation of capacitance between frequencies indicates a deviation from an ideal capacitor (Figure S9), emphasizing the difficulties in extracting a well-defined analysis from impedance measurements for these porous PFO films. Under these circumstances, the V_{fb} of PFO_600 °C was found to be $+1.67\ V_{RHE}$ (Figure S9), a high value which is consistent with the high onset potential of $+1.4\ V_{RHE}$ for cathodic photocurrent found on j-V curves. The high V_{fb} confirms the PFO conduction band edge is suitable to provide the required potential for water reduction. The effective carrier (hole) density was calculated to be 1×10^{19} cm^{-3} at 10 Hz.

3. Conclusions

$PrFeO_3$ (PFO) photocathodes were successfully prepared on FTO-ABS glass using a spray pyrolysis method and a solution of nitrate precursors with citric acid. PFO was formed directly on the glass substrate using different calcination temperatures 500, 600 and 700 °C in order to optimize fabrication conditions. X-ray diffraction confirmed the presence of PFO for calcination steps

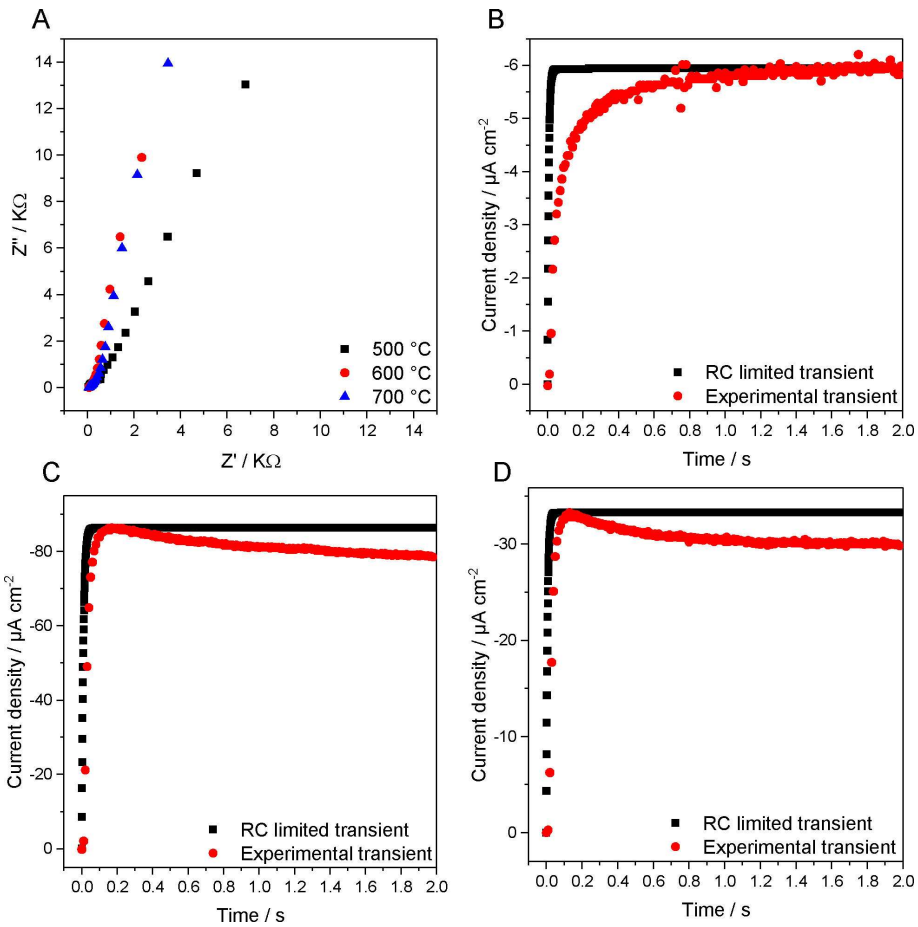

Figure 6. A) EIS measurements used for RC calculations in 0.1 M $NaSO_4$ with a DC of +0.61 V_{RHE} and AC potential frequency range 10^5–0.1 Hz with an amplitude of 5 mV under dark conditions. Experimental transient photocurrent plots from chronoamperometry measurements at +0.61 V_{RHE} under chopped solar illumination with calculated RC limited transients for B) PFO_500 °C, C) PFO_600 °C and D) PFO_700 °C.

of 600 and 700 °C but failed to identify any PFO diffraction peaks at a calcination temperature of 500 °C, suggesting a lack of crystallinity. Photoelectrochemical measurements of these films revealed their ability to generate cathodic photocurrent. On chopped simulated sunlight (1 sun) photocurrents achieved for PFO films calcined at 500, 600 and 700 °C were -17 ± 4, -130 ± 4 and $-101\pm2\,\mu A\,cm^{-2}$ at +0.43 V_{RHE} respectively, where three calcined layers were applied for an optimal photoresponse. Incident photon-to-current conversion efficiency measurements showed efficiencies of 1.2, 6.6 and 2.7% at +0.61 V_{RHE} and 350 nm for calcinations of 500, 600 and 700 °C respectively. This suggests a calcination temperature of 600 °C is optimal for maximized photocurrent and efficiency. RC limited photocurrent comparisons showed a slower rise time for PFO_500 °C (1.25 s) when compared to PFO_600 °C and PFO_700 °C (0.17 and 0.13 s), suggesting an increased density of trap states arising from defects at this temperature, further confirming a higher temperature of 600 °C is beneficial when fabricating these PFO photocathodes. In addition, electrochemically active surface area measurements indicate a decrease in surface area with increasing temperature due to sintering, with values of 0.085, 0.072 and 0.058 $mF\,cm^{-2}$ for 500, 600 and 700 °C respectively. To the best of our knowledge we believe that this is the first demonstration of PFO photocathodes for PEC processes and displays both their advantages and potential in this field. Future work should be devoted to the addition of co-catalysts, hole blocking layers and metal dopants to increase observed photocurrents, efficiencies and selectivity for hydrogen evolution.

Experimental Section

Film Fabrication using Spray Pyrolysis

3 g $Pr(NO_3)_3\cdot6H_2O$ and 2.8 g $Fe(NO_3)_3\cdot9H_2O$ were added to 5.3 g citric acid (1:1:4 molar ratio) in 100 ml distilled H_2O. This was then vigorously stirred for 48 h. This solution was then sprayed onto a transparent conductive substrate slide consisting of FTO-ABS. The slide was sprayed using several up and down motions moving from left to right along the glass for up to 10 times. The resulting films were then calcined at 500, 600 and 700 °C for 2 h. The deposition (spray and calcination) was carried out three times for an optimized photocurrent. These films were named PFO_500 °C, PFO_600 °C and PFO_700 °C.

PEC Measurements

PEC measurements were carried out in a three-electrode PEC quartz cell with working electrode, Pt counter electrode, an Ag/AgCl reference electrode, and a 0.1 M Na_2SO_4 electrolyte of pH 12. A 300 W Xe lamp equipped with an AM1.5G solar simulator filter (LOT Quantum Design) was used with an 8 mm-diameter masked area. The intensity was measured to be 100 mW cm^{-2} determined by the distance to the working electrode (these irradiation conditions are herein referred as "1 sun"). Photocathodes were irradiated from the back, that is, since it produced higher photocurrent. An external potential (provided by Ivium CompactStat) was linearly swept from +0.2 to −1.12 V_{AgCl} at a rate of 20 mV s^{-1} under chopped simulated sunlight. Standard deviations of photocurrents (represented with ±) were calculated out of more than 3 samples with mean values stated.

EIS measurements for RC limited current calculations were carried out in 0.1 M $NaSO_4$ with a DC of −0.3 V_{AgCl} and AC potential frequency range 10^5–0.1 Hz with an amplitude of 5 mV under dark conditions. Experimental transient photocurrents were obtained under chopped simulated sunlight (1 sun) at −0.3 V_{AgCl} with a data collection interval of 0.01 s. These were then compared to the RC limited photocurrent calculated from the general expression [Eq. (1)]:[54]

$$j_{ph} = j_{max}\left[1 - e^{-t/RC}\right] \quad (1)$$

where j_{ph} is the calculated RC limited photocurrent, j_{max} is the maximum photocurrent measured from the experimental transient photocurrent, and t is time.

ECSA measurements were carried out by conducting cyclic voltammetry (CV) between +0.2 to −0.3 V_{AgCl} at varying scan rates between 10 and 200 mV s^{-1}. The capacitive current recorded at −0.03 V_{AgCl} was plotted against scan rate where the gradient is directly proportional to the ECSA [Eq. (2)]:

$$\text{ECSA} \propto C = \frac{dQ/dt}{dE/dt} = \frac{i(E)}{v} \quad (2)$$

where C is the electrochemical capacitance, $i(E)$ is the current measured at potential E and v is the scan rate.[55]

EIS measurements for the creation of Mott-Schottky plots were carried out at various potentials under dark conditions. These were completed at fixed frequencies of 10, 100 and 1000 Hz using the following equation [Eq. (3)]:

$$\frac{1}{c^2} = \frac{2}{A^2 N_D e \varepsilon_0 \varepsilon}\left(V - V_{fb} - \frac{K_b T}{e}\right) \quad (3)$$

where C is the capacitance, A is electrode area, N_D the hole carrier density, e the elemental charge, ε_0 the permittivity of the vacuum, ε the relative permittivity of PFO (1×10^4), V the applied potential, V_{fb} the flat band potential, K_b the Boltzmann constant and T the temperature. The hole carrier density was then calculated using the following equation [Eq. (4)]:

$$N_D = \left(\frac{2}{A^2 e \varepsilon \varepsilon_0}\right)\left(\frac{d(1/C^2)}{d(V)}\right)^{-1} \quad (4)$$

Physical Characterization

UV-Vis spectroscopy analysis was conducted using a Cary Series UV-Vis spectrometer evaluating the F(R) functional for wavelengths between 200 and 800 nm. FE-SEM micrographs were obtained using a JEOL 6301F, with an acceleration voltage of 5 keV. HR-TEM micrographs were acquired using a JEM-2100Plus microscope with 200 kV maximum operating voltage. XRD patterns were obtained from a STOE STADI P double setup, equipped with Mythen detectors, using pure Cu–Kα_1 radiation (λ = 1.540562 Å) with a range of 2θ from 20 to 80°. XPS were taken on a Kratos Axis Ultra DLD system using monochromatic Al Kα X-ray source operating at 150 W (10 mA × 15 kV). Gas chromatography (GC) measurements were conducted on a Shimadzu Nexis GC-2030.

Data access Statement

All data created during this research are openly available from the University of Bath data archive at https://doi.org/10.15125/BATH-00708.

Acknowledgements

Authors would like to thank the EPSRC Centre for Doctoral Training in Catalysis EP/L016443/1. S.E. would like to thank the EPSRC Early Career Fellowship EP/P008097/1. D.J.F. kindly thanks the UK Catalysis Hub for resources and support provided via the membership of the UK Catalysis Hub Consortium and funded by the EPSRC (EP/K014706/1 and EP/K014714/1). XPS data collection was performed at the EPSRC National Facility for XPS ('HarwellXPS'), operated by Cardiff University and UCL, under contract No. PR16195. FE-SEM and HR-TEM micrographs were carried in the Material and Chemical Characterisation Facility (MC^2) at the University of Bath by Philip Fletcher.

Keywords: perovskite phases · photocatalysis · photoelectrochemistry · $PrFeO_3$ · spray pyrolysis

[1] B. Sorenson, *Hydrog. Fuel Cells* **2012**, pp. 95–200.
[2] D. Pham Minh, T. J. Siang, D.-V. N. Vo, T. S. Phan, C. Ridart, A. Nzihou, D. Grouset, *Hydrog. Supply Chain.* **2018**, 111–166.
[3] A. Fujishima, K. Honda, *Nature* **1972**, *238*, 37–8.
[4] X. Cheng, Y. Zhang, H. Hu, M. Shang, Y. Bi, *Nanoscale* **2018**, 3644–3649.
[5] C. Mahala, M. D. Sharma, M. Basu, *New J. Chem.* **2019**, 7001–7010.
[6] G. Dayal, P. S. Bassi, T. Sritharan, L. H. Wong, *J. Phys. D* **2018**, *51*.
[7] P. Tang, J. Arbiol, *Nanoscale Horiz.* **2019**, Advance Article.
[8] F. F. Abdi, R. Van De Krol, *J. Phys. Chem. C* **2012**, *116*, 9398–9404.
[9] S. S. Kalanur, Y. J. Hwang, S. Y. Chae, O. S. Joo, *J. Mater. Chem. A* **2013**, *1*, 3479–3488.
[10] C. Jiang, A. Savio, J. A. Moniz, A. Wang, T. Zhang, J. Tang, *Chem. Soc. Rev.* **2017**, *46*, 4645–4660.
[11] Q. Huang, X. Xiao, J. Mater, *Chem. A* **2015**, *3*, 15824–15837.
[12] C. G. Morales-Guio, S. D. Tilley, H. Vrubel, M. Grätzel, X. Hu, *Nat. Commun.* **2014**, *5*, 1–7.
[13] S. Ida, K. Yamada, T. Matsunaga, H. Hagiwara, Y. Matsumoto, T. Ishihara, *J. Am. Chem. Soc* **2010**, 132, 17343–17345.
[14] A. Paracchino, V. Laporte, K. Sivula, M. Grätzel, E. Thimsen, *Nat. Mater.* **2011**, *10*, 456–461.
[15] Z. Zhang, P. Wang, *J. Mater. Chem.* **2012**, *22*, 2456–2464.
[16] Y. X. Yu, L. Pan, M. K. Son, M. T. Mayer, W. De Zhang, A. Hagfeldt, J. Luo, M. Grätzel, *ACS Energy Lett.* **2018**, *3*, 760–766.
[17] W. Wang, M. O. Tade, Z. Shao, *Chem. Soc. Rev.* **2015**, *44*, 5371–5408.
[18] G. E. Eperon, V. M. Burlakov, P. Docampo, A. Goriely, H. J. Snaith, *Adv. Funct. Mater.* **2014**, *24*, 151–157.

[19] I. Poli, J. Baker, U. Hintermair, T. M. Watson, M. Regue, S. Eslava, S. Kumar, E. V. Sackville, P. J. Cameron, *Nat. Commun.* **2019**, 1–10.
[20] L. Gao, *Chem. Commun.* **2018**, *54*, 11459–11462.
[21] J. Shi, L. Guo, *Prog. Nat. Sci.* **2012**, *22*, 592–615.
[22] W. J. Yin, B. Weng, J. Ge, Q. Sun, Z. Li, Y. Yan, *Energy Environ. Sci.* **2019**, *12*, 442–462.
[23] E. Freeman, S. Kumar, V. Celorrio, M. S. Park, J. H. Kim, D. J. Fermin, S. Eslava, *Sustain. Energy Fuels* **2020**, 4, 884–894.
[24] P. Kanhere, J. Zheng, Z. Chen, *Int. J. Hydrogen Energy* **2012**, *37*, 4889–4896.
[25] K. Iwashina, A. Kudo, *J. Am. Chem. Soc.* **2011**, *133*, 13272–13275.
[26] P. Yilmaz, D. Yeo, H. Chang, L. Loh, S. Dunn, *Nanotechnology* **2016**, *27*, 345402.
[27] C. Ederer, N. A. Spaldin, *Phys. Rev. B* **2005**, *71*, 224103.
[28] S. J. A. Moniz, C. S. Blackman, P. Southern, P. M. Weaver, J. Tang, C. J. Carmalt, *Nanoscale* **2015**, *7*, 16343–53.
[29] X. Ren, H. Yang, S. Gen, J. Zhou, T. Yang, X. Zhang, Z. Cheng, S. Sun, *Nanoscale* **2015**, *8*, 752–756.
[30] K. M. Parida, K. H. Reddy, S. Martha, D. P. Das, N. Biswal, *Int. J. Hydrogen Energy* **2010**, *35*, 12161–12168.
[31] G. P. Wheeler, V. U. Baltazar, T. J. Smart, A. Radmilovic, Y. Ping, K.-S. Choi, *Chem. Mater.* **2019**, *31*, 5890–5899.
[32] G. S. Pawar, A. A. Tahir, *Sci. Rep.* **2018**, *8*, 1–9.
[33] Q. Peng, B. Shan, Y. Wen, R. Chen, *Int. J. Hydrogen Energy* **2015**, *40*, 15423–15431.
[34] M. I. Díez-García, V. Celorrio, L. Calvillo, D. Tiwari, R. Gómez, D. J. Fermín, *Electrochim. Acta* **2017**, *246*, 365–371.
[35] Y. Chen, D. Wang, H. Qin, H. Zhang, Z. Zhang, G. Zhou, C. Gao, J. Hu, *J. Rare Earths* **2019**, *37*, 80–87.
[36] H. Huang, L. Lv, F. Xu, J. Liao, *Microchim. Acta* **2017**, 4141–4149.
[37] P. Tang, X. Xie, H. Chen, C. Lv, Y. Ding, *Ferroelectrics* **2019**, *546*, 181–187.
[38] S. N. Tijare, S. Bakardjieva, J. Subrt, M. V Joshi, S. S. Rayalu, S. Hishita, N. Labhsetwar, *J. Chem. Sci.* **2014**, *126*, 517–525.
[39] C. Glynn, C. O'Dwyer, *Adv. Mater. Interfaces* **2017**, *4*, 1600610.
[40] V. Celorrio, L. Calvillo, G. Granozzi, A. E. Russell, D. J. Fermin, *Top. Catal.* **2018**, *61*, 154–161.
[41] V. Celorrio, L. Calvillo, E. Dann, G. Granozzi, A. Aguadero, D. Kramer, A. E. Russell, D. J. Fermín, *Catal. Sci. Technol.* **2016**, *6*, 7231–7238.
[42] G. P. A. Gobaille-Shaw, V. Celorrio, L. Calvillo, L. J. Morris, G. Granozzi, D. J. Fermín, *ChemElectroChem* **2018**, *5*, 1922–1927.
[43] V. Celorrio, E. Dann, L. Calvillo, D. J. Morgan, S. R. Hall, D. J. Fermin, *ChemElectroChem* **2016**, *3*, 283–291.
[44] V. Celorrio, L. Calvillo, C. A. M. van den Bosch, G. Granozzi, A. Aguadero, A. E. Russell, D. J. Fermín, *ChemElectroChem* **2018**, *5*, 3044–3051.
[45] K. Persson, "*Materials Data on PrFeO3 (SG:62) by Materials Project*," DOI 10.17188/1207439can be found under https://www.osti.gov/dataexplorer/biblio/1276430-materials-data-res2-sg-materials-project, **2014**.
[46] L. Ma, S. Y. Ma, X. F. Shen, T. T. Wang, X. H. Jiang, Q. Chen, Z. Qiang, H. M. Yang, H. Chen, *Sens. Actuators B* **2018**, *255*, 2546–2554.
[47] J. Zhang, I. Salles, S. Pering, P. J. Cameron, D. Mattia, S. Eslava, *RSC Adv.* **2017**, *7*, 35221–35227.
[48] A. A. Dubale, C. J. Pan, A. G. Tamirat, H. M. Chen, W. N. Su, C. H. Chen, J. Rick, D. W. Ayele, B. A. Aragaw, J. F. Lee, *J. Mater. Chem. A* **2015**, *3*, 12482–12499.
[49] G. P. Wheeler, K. S. Choi, *ACS Energy Lett.* **2017**, *2*, 2378–2382.
[50] M. S. Prévot, N. Guijarro, K. Sivula, *ChemSusChem* **2015**, *8*, 1359–1367.
[51] X. Sun, D. Tiwari, D. J. Fermin, *J. Electrochem. Soc.* **2019**, *166*, H764–H768.
[52] B. V. Prasad, G. N. Rao, J. W. Chen, D. S. Babu, *Solid State Sci.* **2012**, *14*, 225–228.
[53] A. Hankin, F. E. Bedoya-Lora, J. C. Alexander, A. Regoutz, G. H. Kelsall, *J. Mater. Chem. A* **2019**, *7*, 26162–26176.
[54] Q. Zhang, V. Celorrio, K. Bradley, F. Eisner, D. Cherns, W. Yan, D. J. Fermín, *J. Phys. Chem. C* **2014**, *118*, 18207–18213.
[55] B. K. Kang, G. S. Han, J. H. Baek, D. G. Lee, Y. H. Song, S. Bin Kwon, I. S. Cho, H. S. Jung, D. H. Yoon, *Adv. Mater. Interfaces* **2017**, *4*, 1–8.

Manuscript received: November 28, 2019
Revised manuscript received: February 1, 2020
Accepted manuscript online: February 10, 2020

ARTICLES

Photo finish: $PrFeO_3$ photocathodes are investigated for their photoelectrochemical properties. Using a spray pyrolysis method, an optimal calcination temperature of 600 °C is found and a photocurrent of -130 μA cm^{-2} is achieved, with a high cathodic onset of + 1.4 V_{RHE}.

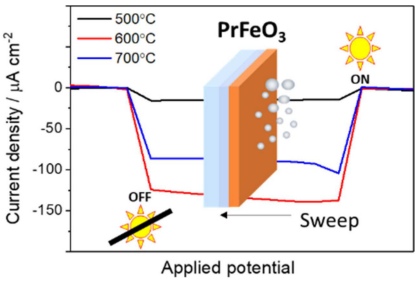

*E. Freeman, Dr. S. Kumar, S. R. Thomas, H. Pickering, Prof. Dr. D. J. Fermin, Dr. S. Eslava**